Review Article

Beyond T2 and 3T: New MRI techniques for clinicians

Benjamin R. Knowles [a],*, Florian Friedrich [a,b], Carola Fischer [a,b], Daniel Paech [c], Mark E. Ladd [a,b]

[a] Medical Physics in Radiology, German Cancer Research Center (DKFZ), Heidelberg, Germany
[b] Department of Physics and Astronomy, University of Heidelberg, Heidelberg, Germany
[c] Department of Radiology, German Cancer Research Center (DKFZ), Heidelberg, Germany

ARTICLE INFO

ABSTRACT

Technological advances in Magnetic Resonance Imaging (MRI) in terms of field strength and hybrid MR systems have led to improvements in tumor imaging in terms of anatomy and functionality. This review paper discusses the applications of such advances in the field of radiation oncology with regards to treatment planning, therapy guidance and monitoring tumor response and predicting outcome.

© 2019 The Authors. Published by Elsevier B.V. on behalf of European Society for Radiotherapy and Oncology. This is an open access article under the CC BY-NC-ND license (http://creativecommons.org/licenses/by-nc-nd/4.0/).

1. Introduction

Magnetic Resonance Imaging (MRI) is an established and valuable tool in radiation oncology for providing information regarding treatment planning and measuring treatment response. The main strengths of MRI are for visualizing soft tissue, as well as providing biological and functional information such as tissue perfusion and diffusion without the need for ionizing radiation.

Despite the incorporation of these MRI-based techniques, there are still many cancers for which there is a very poor clinical outcome for the patient. Continuing technological advances, however provide the opportunity for MRI to play a greater role in cancer treatment, as new techniques emerge that have the potential to further inform the clinician in the treatment process or aid therapy.

A significant and continuing trend is the availability of MRI scanners with even higher field strength than 3T. As MRI scanners increase in field strength, the enhanced sensitivity and emergent contrast mechanisms imply that improved imaging biomarkers for treatment response become clinically feasible. Furthermore, with the advent of hybrid MRI-linac systems in the clinical setting, MRI can be utilized to directly guide treatment through novel sequence development and reconstruction. Thus, new opportunities arise for therapy planning and monitoring. However, the use of these systems in the radiotherapy setting requires a thorough

validation. Compared to clinical MR scanners, at higher fields strengths changes in the T_1, T_2 and T_2^* times of tissue affects image contrast, and the larger off-resonance effects increase image distortions, which may affect accuracy in tumor delineation. On hybrid MR-linac systems, issues regarding therapy guidance arise from the rate at which it is possible to acquire MR images, thus accurately capturing motion with minimal latency.

In this paper, new potential clinical tools that have become relevant through new MRI hardware and their challenges and applications in radiation oncology will be reviewed.

2. Ultrahigh field MRI in radiation oncology

Ultrahigh field (UHF) MRI is considered to be at static magnetic field strengths of 7T or higher. Until recently, UHF imaging has been an interesting research tool; however, the first 7T MRI scanner with CE [1] and FDA [2] approval has been released, allowing for the possibility of UHF MRI to enter clinical routine. UHF-MRI has advantages and disadvantages, which are discussed in detail here [3]. One of the clear benefits of UHF MRI is the increased sensitivity, quantified as signal-to-noise ratio (SNR), which has an approximately linear relationship with the main magnetic field strength, which, at field strengths above approximately 3T, the increase in SNR is greater than linear [4]. The increase in SNR can be used to increase spatial resolution $\Delta x^3 \propto (1/\text{SNR})$, allowing for sharper images and increased visibility of finer structures. One field in which the increased sensitivity of UHF MRI is particularly valuable is in non-^{1}H imaging. As the human body is mostly composed of water, H_2O, ^{1}H or proton imaging of water provides the

largest MR signal; however, in theory imaging with any nucleus with a nuclear spin > 0 is possible. The MR applications of non-^{1}H, isotopes, which are termed the X-nuclei, are reviewed in detail in Section 2.2. For magnetic resonance spectroscopy (MRS), utilizing either ^{1}H or X-nuclei, the higher field strength not only provides higher sensitivity, but also increases spectral resolution and allows for the detection of more metabolites [5].

One of the disadvantages of UHF ^{1}H imaging, is that the wavelength of the applied excitation field is short enough that the electromagnetic wave effects can no longer be ignored, meaning that uniform radiofrequency (RF) excitation at UHF strengths becomes increasingly difficult. This issue most commonly manifests as areas of large signal heterogeneity within the FOV. As the FOV increases, the RF heterogeneity becomes more pronounced and consequently, progress in whole-body imaging at UHF has been slower than neurological applications [6]. A further disadvantage of UHF MRI is that the RF energy is absorbed into tissue at a higher rate than at lower field strengths. The regulatory limits imposed on this rate of energy absorption, the Specific Absorption Rate (SAR), given in W/kg, are the same for all field strengths, but at higher fields these limits are reached at comparatively lower excitation flip angles, so that significant adjustments to some imaging sequences are necessary. Additionally, due to the shorter RF wavelength and more complex RF interactions at UHF, localized heating can occur and must be numerically simulated [7] in order to apply appropriate safety limits.

The issues around RF heterogeneity and SAR can be alleviated by application of multichannel RF systems, a technique known as parallel transmission. In such systems, multiple RF pulses are applied simultaneously though a dedicated multichannel transmit coil. Many different techniques have been proposed, in which the phases, and amplitudes can be adjusted on each channel in order to produce a more uniform RF excitation, such as B1+ shimming [8,9], SPOKES [10], k-T points [11] and SPIral Non Selective (SPINS) RF Pulses [12]. There are also additional methods requiring no user interaction such as universal pulses [13] and Time Interleaved Acquisition of MOdes (TIAMO) [14].

2.1. Treatment planning

The greatest progress in UHF MRI research has been in neurological applications, which due to the smaller size of the FOV suffer less from the effects of the heterogeneous RF excitation field. Most often the field variations are not accounted for or some compensation can be provided through the use of dielectric pads inserted in the RF coil [15], as the high permittivity of the dielectric material pulls the RF excitation pattern towards the pad.

Radiotherapy often incorporates information from MRI into the planning process, with the requirements for planning including good tumor delineation, with robust image quality and high contrast-to-noise ratio (CNR) [16]. The contrast provided by T_2 weighted imaging is well established in radiotherapy planning [17]. Images are typically acquired using turbo spin echo (TSE) or a variant thereof. TSE is energy intensive due to the application of a train of 180° refocusing pulses, quickly leading to SAR limitations at UHF strengths. One of the standard clinical sequences, FLuid-Attenuated Inversion-Recovery (FLAIR) [18], has widespread use in therapy planning of brain tumors [19], and has been successfully demonstrated at 7 T [20–24], necessitating however several modifications. To minimize SAR by reducing the peak RF amplitude, the duration of the pulses can be extended, or VariablE-Rate Selective Excitation (VERSE) can be applied [25]. To minimize SAR within the readout train, hyperechoes [26] and a low flip angle variant of TSE, SPACE [27], have been applied. Due to the altered T_1 relaxation times at higher fields, the FLAIR contrast was found to be reduced at higher field strengths, although

it can be recovered by the employment of T_2 preparation at the start of the sequence [20].

Recent studies have investigated the role of UHF in radiotherapy planning, in particular the role of FLAIR [21], where images from glioblastoma patients at 7T and 3T were compared as shown in Fig. 1. Results suggested that the higher spatial resolution improves visualization of the white matter tracts, which are known infiltration routes of glioblastoma [28].

The technical feasibility of integrating 7T MR images into the treatment planning of brain tumor patients was explored in [29] using healthy volunteers, in which images were assessed on a qualitative basis, as well as for geometric distortions. Geometric distortions were further assessed in [30], in which the geometric accuracy of images at 3T and 7T were compared. Distortions were found to be higher at 7T compared to 3T, but were still considered to be within acceptable limits for therapy planning. A similar conclusion was also reached in [31], in which 7T images were assessed for geometrical distortions with regards to image guidance in neurosurgery.

2.2. Measuring treatment response at UHF

Currently, clinical measures to treatment response rely on anatomical changes in the tumor, such as the RECIST (Response Evaluation Criteria In Solid Tumors) criteria [32]; however, this approach cannot detect or describe early cellular alterations in response to therapy, which can take up to months after therapy to manifest morphologically [33].

Many MR-based surrogate biomarkers have been linked with treatment outcome, such as dynamic contrast-enhanced (DCE) MRI [34] and diffusion-weighted imaging (DWI) [35]. The limitation of contrast enhanced MRI is that it only visualizes disruptions in the Blood Brain Barrier, and so does not provide information in areas of non-enhancing tumor [36,37].

The apparent diffusion coefficient (ADC) is the most common DWI-derived imaging biomarker with broad clinical applications. The majority of studies show an inverse correlation between the ADC and tumor cellularity [38–41]. With regards to therapy response assessment, changes in the ADC have been shown to be associated with treatment response in glioma patients early after radiation therapy, with these changes being hypothesized to be linked to cellular structure reflecting apoptosis or necrosis [35,42,43].

Advances in UHF MRI open up the potential to investigate additional biomarkers. In clinical MRI, ^{1}H is the nucleus that is predominately measured, as ^{1}H is associated with imaging water. As water is the main component of the human body, it is from water that the largest MR signal is generated. However, other sources of signal apart from water are achievable with MRI. In the case of MR imaging of nuclei other than standard water protons (^{1}H), termed the X-nuclei, new insights into cellular function and metabolism may be accessible. Unlike ^{1}H imaging, the X-nuclei allow for a more direct imaging of physiological processes, including biomarkers for treatment response that may provide information complementary to that obtainable by PET. X-nuclei can in principle be imaged on any MRI system; however, they have a relatively low abundance and therefore an SNR of several orders of magnitude lower then ^{1}H [44]. UHF MRI and the development of SNR-optimized, ultrashort echo time (UTE) sequences [45–50] have allowed research involving the X-nuclei to advance to a level where the clinical impact can be realistically assessed. In addition, spectroscopic techniques that facilitate the imaging of ^{1}H nuclei bonded to other molecules, other than water also benefit from higher sensitivity at UHF. Techniques such as Chemical Exchange Saturation Transfer (CEST) enable imaging of a subset of these molecules and also
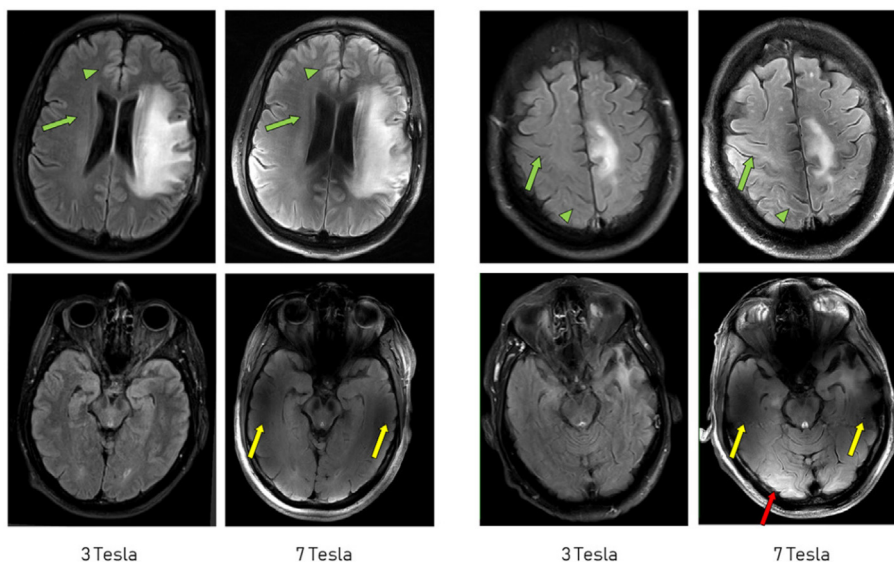
Fig. 1. FLAIR images in a glioblastoma patient at 3T and 7T [21]. Green arrows show the major white matter tracts, green arrowheads show the boundary between grey and white matter, and the yellow arrows show areas of signal loss at 7T corresponding to RF non-uniformity. (For interpretation of the references to colour in this figure legend, the reader is referred to the web version of this article.)

benefit strongly from the increased spectral resolution associated with UHF MRI.

In the following sections, several X-nuclei and CEST applications in the context of radiation therapy are described.

2.2.1. Sodium-23 imaging

Sodium (^{23}Na) has an important role in cell physiology [51]. With normal cell function, a large concentration gradient exists between the intra- and extracellular spaces, with the extracellular concentration being a factor of 10 higher than the intracellular concentration. This gradient is maintained by an energy dependent sodium-potassium pump (Na$^+$/K$^+$-ATPase), so that any disturbances in the cell metabolism or membrane manifest as an increase in the intracellular ^{23}Na concentration.

In oncology, a change in the intracellular ^{23}Na concentration is a biomarker for tumor malignancy [52–56], and cellular viability [57], and has shown promise as an indicator of treatment response. This has been demonstrated in animal models [58,59], and more recently in glioblastoma patients measured at 3T [60] and 7T [61].

2.2.2. Oxygen-17 imaging

The Warburg effect [62] is a phenomenon in which cancer cells are observed to metabolize glucose via the less efficient glycolysis pathway, producing lactate, in contrast to oxidative phosphorylation, in which glucose is metabolized with oxygen [63]. This change in metabolic pathway occurs even in the presence of sufficient oxygen.

Using PET with the glucose analog ^{18}F-fluorodeoxyglucose (FDG) has become the clinical standard for imaging many malignant tumors [64]. FDG PET has found applications in tumor detection and staging [65], as well as in characterizing response to chemotherapy and radiotherapy [66–68].

A drawback to using FDG PET for measuring Cerebral Metabolic Rate of Oxygen consumption (CRMO$_2$), and tumor characterization in general, is that FDG is not a specific tracer. Glucose is metabolized in all cells, and although in most cases cancer cells have a higher metabolic activity, this is not always the case, for example in prostate cancers. As a result, FDG PET is challenged by low specificity [69].

As an alternative to FDG PET, ^{15}O-labeled water (H$_2^{15}$O) can be used as the PET tracer, allowing for a direct measurement of CRMO$_2$ [70,71] that is more specific to the Warburg effect. Although, ^{15}O PET is considered the gold standard for imaging CRMO$_2$, it is costly to apply in the clinical setting, as ^{15}O has a short half-life ($t_{\frac{1}{2}} = 123$ s) and requires an on-site cyclotron for generation [71]. Despite technical and financial challenges, ^{15}O PET has been used to show reduced levels of CRMO$_2$ in tumors [72–76], which is particularly pronounced in high grade tumors [77].

MRI can also be used to image the same effect, through the use of the only stable isotope of oxygen, ^{17}O, that produces an MR signal. ^{17}O is a stable, non-radioactive isotope, but when compared to ^{1}H (proton) MRI, ^{17}O has a low natural abundance (0.037%) and a low gyromagnetic ratio, leading to a sensitivity of 2.9% compared to ^{1}H [78], for an overall *in vivo* signal sensitivity approximately 20,000 times smaller than ^{1}H. At this low sensitivity, ^{17}O imaging benefits from UHF MRI, and additional higher concentrations of ^{17}O are typically inhaled to increase SNR, although research on imaging naturally abundant ^{17}O has been performed [79].

The first reported usage of ^{17}O was as an agent to shorten the T_2 of ^{1}H [80], followed closely by MRS detection [81]. Usage of ^{17}O was reported in a preclinical experiment [82], and in natural abundance imaging [83]. It was not until the introduction of UHF MRI however, that significant human *in vivo* studies occurred [84,85]. The first clinical demonstration of CRMO$_2$ determination was in a glioblastoma patient [86], shown in Fig. 2, using an efficient, MR-compatible breathing system [87]. Inhaled ^{17}O gas is not visible in the MR images until mitochondrial conversion to water, providing a direct, quantitative measure of CRMO$_2$. Reproducibility of CRMO$_2$ measurements has been investigated in healthy subjects [88], and the same method was applied in two glioma patients [89].

2.2.3. Phosphorous-31 spectroscopy

Phosphorous (^{31}P) plays a role in detecting all metabolites involved in energy metabolism, as well as being able to indirectly measure tissue pH, using the Henderson-Hasselbalch equation [44], in which pH is related to the chemical shift of the inorganic phosphate peak compared to other peaks. The acidity of the cellular environment is a known influence on the response of a tumor to treatment [90]. The NMR spectrum of ^{31}P has multiple peaks,
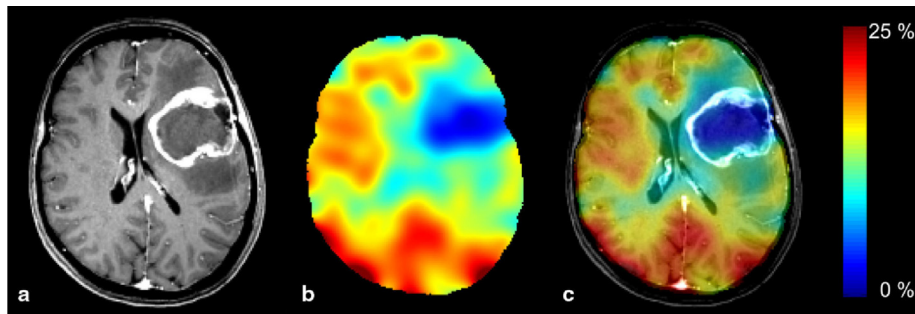
Fig. 2. (a) MP-RAGE, (b) relative ^{17}O maps and (c) overlay in a glioblastoma patient [87].

making the detection of ^{31}P most suitable for spectroscopy, or spectroscopic imaging, although direct imaging is possible [91,92].

An advantage of, ^{31}P MRS is that ^{31}P has a high natural abundance *in vivo* and relatively high MR sensitivity (7% of the ^{1}H signal based on gyromagnetic ratio [44]), making the detection of this nucleus feasible even at lower, clinical field strengths. Nevertheless, ^{31}P detection has shown improvements at higher field strengths. Due to the increased SNR, 3D spectroscopic imaging can be acquired in clinically feasible scan time [93], and at higher field strengths, ^{31}P spectroscopy benefits from increased spectral resolution, allowing for the detection of finer structures in the ^{31}P spectra [94].

UHF field strengths have brought a significant improvement to ^{31}P spectroscopy in the prostate [95] for the detection of metabolites in prostate cancer [96]. On observation of the ^{31}P spectra, differences in the phosphomonoester (PME) to phophocreatine (PCr) ratio, PME to β-ATP ratio and the PCr to β-ATP ratio have been linked to the distinction between healthy and cancerous tissue [97,98]. Using the improved spectral resolution at 7T, the split NMR peaks of phosphocholine (PC) and phosphoethanolamine (PE) as well as their glycerol derivatives (GPC and GPE respectively) can be detected. These compounds are related to phosphoid metabolism, and the distinction of which has been linked to tumor malignancy [99]. To date, several studies have demonstrated ^{31}P spectroscopic imaging at 7T with custom-made transceive coils [100–104], and were successfully able to detect the phosphoid peaks in the prostate.

2.2.4. Carbon-13 and deuterium spectroscopy

As almost all compounds involved in metabolism contain carbon, which allows for the detection of metabolites such as glucose, pyruvate and lactate with MRS [44]. The challenge of carbon detection under MRS is that the only stable isotope of carbon, carbon-13 (^{13}C), has a very low natural abundance of 1.1% and therefore a very low *in vivo* sensitivity. Nevertheless, MRS can be performed using the natural abundance of ^{13}C, albeit with long acquisition times for a number of applications, such as glyocen measurements [105]. More common however, is to administer a ^{13}C-labeled substrate such as [1-^{13}C]glucose and observe the metabolic pathways by detection of the resulting metabolites [106]. In oncology, the administration of [1-^{13}C]glucose can be used to detect lactate tumors directly on account of the altered glucose metabolism [107,108], an underlying characteristic of the Warburg effect.

To overcome limitations of low ^{13}C sensitivity, nuclear hyperpolarization is a technique that has the potential to increase of the signal of nuclei such as ^{13}C by several orders of magnitude. The most prominent 13C hyperpolarization techniques for ^{13}C are dissolution Dynamic Nuclear Polarization (dDNP) [109], or parahydrogen synthesis (PASADENA) [110]. The metabolic pathways of hyerpolarized [1-^{13}C]pyruvate have been applied to glioma in a mouse model [111], and prostate cancer in a human study [112].

Hyperpolarized ^{13}C MRS has been used as a biomarker for treatment response. [1-^{13}C]pyruvate is promising for the detection of early change in lymphoma cells after chemotherapy in mouse models, [113], as well as changes due to anti-VEGF treatments [114]. Furthermore, hyperpolarized [1-^{13}C]pyruvate MRS has been demonstrated as a surrogate for measuring reactive oxygen species [115], which has potential for real-time assessment of tissue response to ionizing radiation.

An alternative to ^{13}C MRS is to label the metabolite with Deuterium (^{2}H), which was recently presented as a novel approach for imaging metabolism and the Warburg effect. First theorized in 1935 [116], experimental validation has required UHF MRI in order to overcome the inherently low sensitivity of this technique. To date, ^{2}H-MRS has been performed [117] as well as ^{2}H spectroscopic imaging [118], allowing for absolute maps of glucose, pooled glutamate and glutamine (Glx) as well as lactate to be acquired.

2.2.5. CEST

Chemical Exchange Saturation Transfer (CEST) is an imaging technique in which protons bound to metabolites such as proteins, amino acids and lipids are amplified. These metabolites resonate at a different frequency compared to that of ^{1}H nuclei in water, but are nevertheless detectable with ^{1}H MRI. The application of a saturation RF pulse targeted at the appropriate resonant frequency, or frequency range, can reduce the MR signal of ^{1}H bound to a certain chemical species. These bound protons are in constant exchange with free water protons; the saturated ^{1}H protons exchange with the free water ^{1}H nuclei, and therefore become detectable by ^{1}H MRI as a signal loss in the ^{1}H water images. Furthermore, as this exchange is ongoing, the number of saturated protons becoming water protons increases with the duration of the applied saturation RF pulse, amplifying the detectable MR signal by a factor on the order of 100–1000 if the T_1 relaxation times are suitably long [119].

Of particular relevance with regard to tumor imaging is the detection of two metabolite signals known to have links to protein content: Amide Proton Transfer (APT) [120], and the relayed Nuclear Overhauser Effect (rNOE) [121]. Both of these have been shown to be correlated with brain tumor grade [122–127]. Additionally, APT mediated CEST MRI has been shown to be associated with the isocitrate dehydrogenase (IDH)-mutation status in newly-diagnosed gliomas [128,127]. Further studies have investigated the use of CEST imaging as an indicator of treatment response in glioma patients, and indicate that CEST could play an important role as an early measurement of treatment response [129–135], as shown in Fig. 3 with recent studies reporting the use of CEST to distinguish between therapy responders and non-responders during [131] or directly after [132] therapy. Recently, an association between CEST and long-term outcome by means of patient
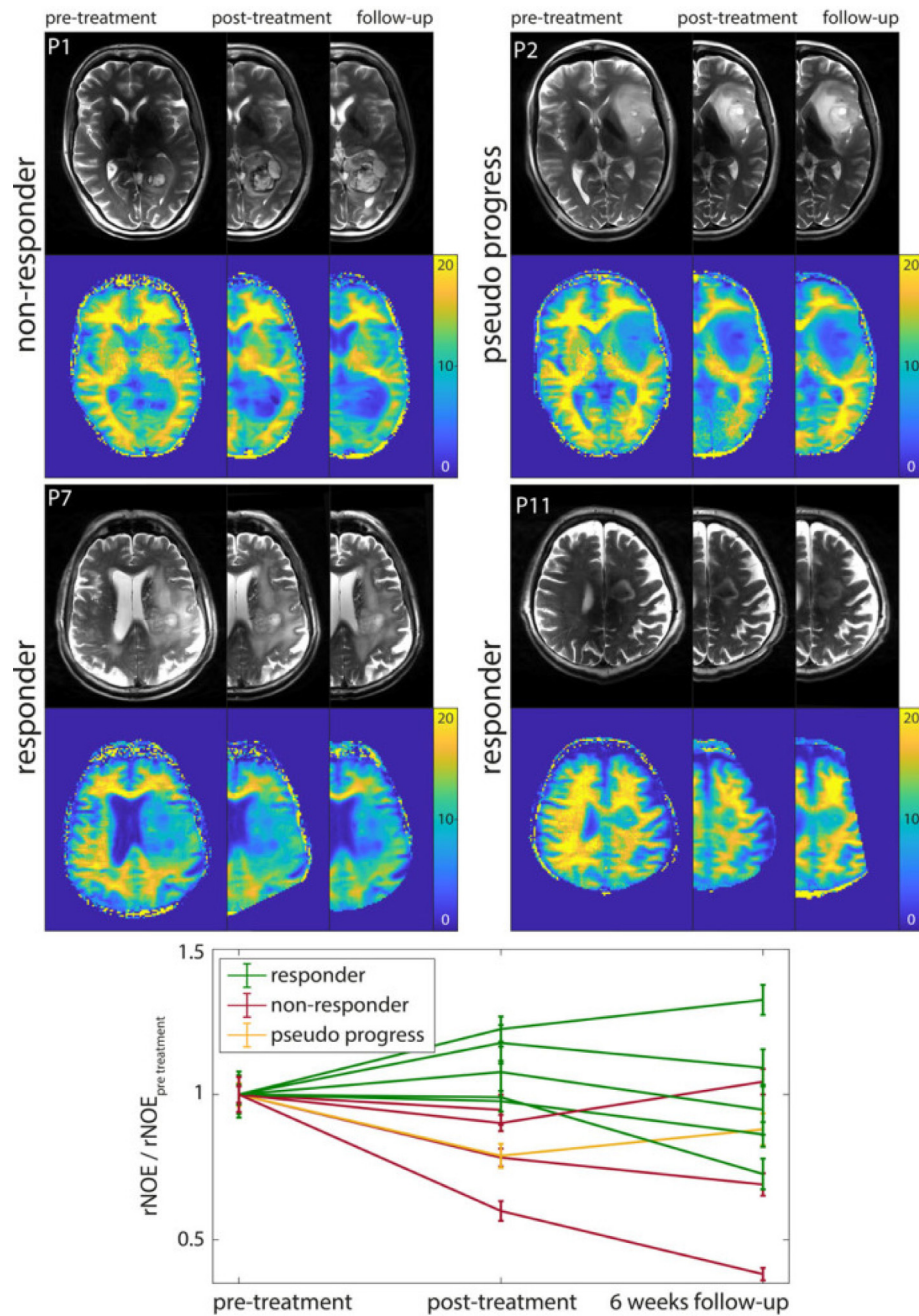
Fig. 3. rNOE-CEST as a measure of treatment response in glioma patients [132].

overall survival and progression-free survival could be shown [136].

Besides imaging of endogenous metabolites, chemical exchange sensitive MR techniques also have the potential to detect exogenously administered substances containing exchangeable protons. A promising substance for such a new type of contrast agent is natural D-glucose, since it can be detected through chemical exchange saturation transfer (CEST) [137–139] or chemical exchange sensitive spin-lock (CESL) [140–142]. The feasibility of dynamic glucose-enhanced (DGE)-MRI in humans has recently been demonstrated in independent studies employing both CEST and CESL-based techniques [141–144]. The signal origin of DGE MRI seems to be dominated by tissue perfusion but still needs further investigation.

3. MR-guided radiotherapy

Intrafractional motion causes the radiation delivery to the target volume to be blurred over the path of motion and is a serious issue for the treatment of all thoracic and abdominal tumors, in particular, lung tumors [145]. Radiation treatment of central lung carcinoma poses a risk of toxicity [146], making localized irradiation in the lungs crucial. Liver metastasis treatment benefits from high dose [147], which makes guidance important to prevent side-effects. Tumor motion occurs mainly in the superior-inferior direction, but also components of left-right and anterior-posterior motion can occur [145].

Several methods are currently available to compensate for intrafractional motion. Breathing control methods include

breath-holding, in which dose delivery occurs while the patient consciously halts respiration for a short period of time, or techniques such as forced shallow breathing using abdominal compression [148]. A second common method is to use respiratory gating, in which dose is delivered during a certain portion of the breathing cycle. This method requires measurement of respiration, which can be achieved using internal fiducial markers under X-ray guidance [149], external markers on the skin surface or image-based tracking from video [150]. Breathing control and gating both have disadvantages. Breath-holding may not be reproducible, and patients can be non-compliant. With gating methods, patients can require some coaching to breathe effectively, and in addition, therapy duration increases as the dose is only delivered during certain time periods. Furthermore, when surrogates are used for motion measurement, there is the potential that the surrogate does not accurately represent the motion of the tumor [151–153]. The most desirable method of motion compensation is to directly track the tumor position and concurrently update the linac multi-leaf collimator (MLC) in real-time. To achieve this, tumors have been imaged under X-ray fluoroscopy [154]; however, tumor delineation is limited using this imaging modality. Alternative to directly imaging the tumor under fluoroscopy, it is possible to track internal fiducial markers [155] for real-time MLC updates. The theoretical benefits of real-time tumor tracking would be to reduce or eliminate the need for a safety margin for motion during planning, while simultaneously applying the X-ray beam at 100% duty cycle.

Recent advances in MR technology not only provide new opportunities for therapy planning and monitoring, they also open up new paths for direct, MR-guided radiotherapy. In particular is the availability of hybrid MR-linac systems which combine magnetic resonance imaging with a linear accelerator, are expected to have a large impact on radiotherapy treatment planning and intra/ inter-fractional tumor tracking.

Commercial MR-linac systems are now available: MRIdian (ViewRay, OH, USA) [156,157] and Elekta Unity (Elekta AB, Stockholm, Sweden) [16,158–160], as well as research systems in Edmonton, Canada (MagnetTx) [161,162] and Sydney, Australia [163,164]. Techniques in real-time MRI can be applied to monitor tumor position and compensate for intrafractional motion with the high soft-tissue contrast associated with MRI. These techniques are reviewed in the following sections.

3.1. Real-time techniques in MR imaging

In the ideal case, MRI can be used to acquire a 3D volume that encapsulates the entire tumor, that allows for full 3D characterization of tumor position and shape. However, as MRI is a relatively slow imaging modality, 3D real-time MRI is still limited in capability. Echo-planar imaging (EPI) is one technique has been applied to 3D imaging. Echo volumar imaging (EVI) [165] is a single-shot EPI technique that can acquire a 3D volume in approximately 100 ms. In more recent implementations, variants of EVI have been applied in image navigation [166] and 3D fMRI [167], using segmented readouts or multi-slab fMRI [168] in which the image acquisition is distributed over a number of repetition times, leading to acquisition times of approximately 0.5–1 s. EPI acquisition has a number of disadvantages. The long read-out duration of these sequences introduces a large dependence on T_2^* and non-uniformity in the main magnetic field, which can cause large geometric distortions in the images. Consequently image resolution is necessarily low to minimize the read-out duration. Furthermore, as magnetic field variations are more pronounced in the thorax and abdomen than in the brain, EPI is very limited in whole-body applications.

Typically, real-time acquisition is acquired in 2D, as is used in cardiac imaging of irregular heart motion [169], interventional MRI [170], joint kinetics [171] and speech analysis [172]. In the case of tumor tracking, balanced steady-state free precession (bSSFP) [173] acquisition techniques are commonly employed, due to good soft tissue contrast and high SNR, which is especially advantageous for MR-linacs, where the main magnetic field is often 1.5T or lower.

For tumor imaging, a single slice is typically acquired at a rate of 3–5 Hz [174–176]. Multiple 2D slices can be interleaved to determine motion in 3D [177–179] at a reduced acquisition rate of approximately 2–3 Hz. Imaging in 1D has also been studied using pencil-beam navigators in order to resolve the main component of motion in the superior-inferior direction [180,181] at a acquisition rate of 30–50 Hz. Full 3D imaging has been implemented as well [182], in which a volume was acquired every 7 s.

Due to the extent to which image acquisition can be accelerated and an inherent robustness against motion artifacts, radial acquisition techniques are often applied in real-time MRI imaging rather than the conventional Cartesian techniques generally applied in diagnostic imaging. Read-out lines can be skipped in radial imaging with a lower impact on image quality [183]. Imaging in 2D at up to 50 Hz has been achieved with a radial encoding scheme [184]. Using a golden angle increment between two adjacent radial profiles enables flexible adaption of the temporal resolution [185]. As with conventional Cartesian imaging, the bSSFP sequence is particularly advantageous for real-time tumor tracking and can be easily combined with fast radial imaging [186].

3.2. Acceleration and image reconstruction

MR imaging is a compromise between temporal and spatial resolution. Nyquist theory imposes limits on the minimum amount of data required to reconstruct an image at a certain spatial resolution. However, many techniques exist that overcome the Nyquist limit in order to accelerate image acquisition by undersampling the required amount of data but maintain a higher spatial resolution. For real-time imaging, this is highly desirable but is not always feasible in implementation, as the consequences of these acceleration techniques are prolonged, often iterative, image reconstruction algorithms. Some acceleration techniques can be employed for real-time imaging with a minimal cost to reconstruction times. These methods acquire undersampled images, but during reconstruction incorporate data from previous frames into the reconstruction of the current frame. View-sharing techniques such as Keyhole [187,188], 3D Time Resolved Imaging of Contrast KineticS (TRICKS) [189] and Time Resolved Echo-shared Angiography Technique (TREAT) [190], have a long-established application in angiography, but have also been applied for 3D imaging of lung tumors at approximately 1 Hz [191,192]. Radial imaging is particularly suited to such view-sharing methods. Using golden angle acquisition methods [185], the reconstruction of a frame can be performed using an arbitrary number of radial profiles, which may have applications in sequences that adapt temporal resolution to the current motion situation [193].

Developments in computer hardware and algorithms, in particular in the area of parallel computing. Accelerated image reconstruction allows additional acquisition techniques to become feasible for real-time imaging. Reconstruction times of Sensitivity Encoding (SENSE) [194] and the related variants for dynamic imaging k-T SENSE [195] and TSENSE [196] have been decreased by a factor of 10–150 by parallelizing sections of the reconstruction on a Graphics Processing Unit (GPU) [197,198], with reconstruction times of approximately 10 ms per 2D image. Similar performance improvements have been observed for radial imaging with GPU implementations of Non-Cartesian SENSE [199], Radial GRAPPA [200] and regularized nonlinear inverse reconstruction [201], shown in Fig. 4.
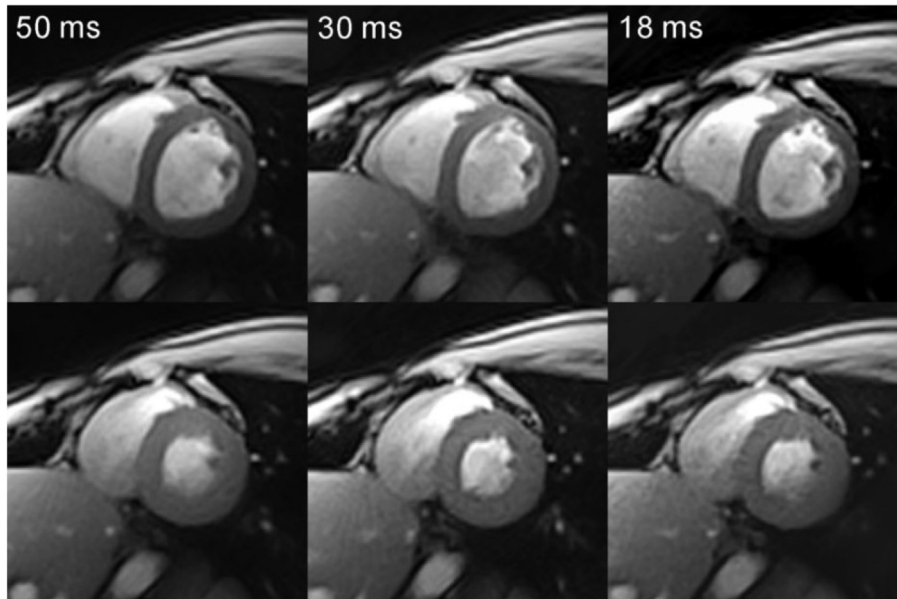
Fig. 4. Real-time images of the heart acquired at diastole and systole at different temporal resolutions [184].

3.3. Tracking and motion modeling

In addition to MR imaging and reconstruction, a real-time measure of tumor position is required in order to update the MLC, or to gate the dose delivery. The most straightforward approach is to derive the position information directly from the MR image. Often used in this case is autocontouring, in which the tumor or organ is automatically delineated [202–210]. Alternative methods include template matching, in which a template shape, for example of an organ or tumor, is located on the dynamic MR images [175,177,211,212], artificial neural networks [175,178] and non-rigid image registration [157]. Although this approach to tumor position determination is robust [213], the limitation of these approaches is that motion can only be derived in-plane.

More advanced tumor tracking methods aim to model the tumor or organ motion to predict 3D motion or to account for system latency that would delay updates to the MLC. A motion model may be constructed from 4D MR or CT images, which can be acquired before therapy and the image data binned according to a measurement of the breathing cycle. As model input, 2D real-time images can be used to estimate 3D motion [214–219], to overcome slow MR image acquisitions [220] or system latencies using filters [221,222] or artificial neural networks [223,224].

4. Future role of MRI in radiation oncology

Radiotherapy has been a part of cancer treatment for the last 100 years, and has constantly evolved as new technologies and scientific understanding have emerged. The introduction of linear accelerators in the 1950s [225] allowed for higher energies and better collimation compared to the previously used radium and cobalt sources. With the introduction of computed tomography (CT) in the 1970s 3D treatment planning became possible and therefore the possibility to perform 3D dose delivery. The introduction of PET and MRI in the 1980s allowed for additional anatomical and functional information to be incorporated into treatment planning as well as valuable information on tumor response to be collected for updating the treatment regimen.

In recent years, improvements in MRI technology and computing hardware have impacted the radiotherapy workflow and pro-

vided new capabilities for refining patient care. As MRI moves toward higher field strengths, imaging of tumor mircoenvironment and metabolism comes closer to being a clinical reality; additionally, the increased spatial resolution allows for visualization of finer anatomical structures. Initial studies investigating the applications of UHF MRI for radiation treatment planning and measuring treatment response have been conducted with promising results. As another important step, MRI is now being incorporated directly into radiotherapy treatment, enabling hybrid MR-Linac systems that can simultaneously track and irradiate tumors. These developments have the potential to dramatically change how tumors in the thorax and abdomen are treated.

The role of MRI promises to increase over the coming years. If the clinical efficacy of these new techniques is proven, such approaches can be translated into the clinical routine, with the potential to strongly impact the outcome of radiotherapy treatments.

Conflict of interest

The authors declared that there is no conflict of interest.

Acknowledgments

References

[1] https://appliedradiology.com/articles/siemens-obtains-first-ce-approval-for-ultra-high-field-7t-mr-scanner; 2017.

[2] https://www.fda.gov/NewsEvents/Newsroom/PressAnnouncements/ucm580154.htm; 2017.

[3] Ladd ME, Bachert P, Meyerspeer M, Moser E, Nagel AM, Norris DG, Schmitter S, Speck O, Straub S, Zaiss M. Pros and cons of ultra-high-field MRI/MRS for human application. Prog Ncl magn Reson Spectrosc 2018;109:1–50.

[4] Pohmann R, Speckm O, Scheffler K. Signal-to-noise ratio and MR tissue parameters in human brain imaging at 3, 7, and 9.4 Tesla using current receive coil arrays. Magn Reson Med 2016;75(2):801–9.

[5] Balchandani P, Naidich TP. Ultra-high-field MR neuroimaging. Am J Neuroradiol 2015;7:1204–15.

[6] Kraff O, Fischer A, Nagel AM, Mnninghoff C, Ladd ME. MRI at 7 Tesla and above: demonstrated and potential capabilities. J Magn Reson Imag 2015;41(1):13–33.

[7] Fiedler TM, Ladd ME, Bitz AK. Sar simulations & safety. Neuroimage 2018;168:33–58.

[8] Ibrahim TS, Lee R, Baertlein BA, Kangarlu A, Robitaille P-ML. Application of finite difference time domain method for the design of birdcage RF head coils using multi-port excitations. Magn Reson Imag 2000;18(6):733–42.

[9] Hoult DI. Sensitivity and power deposition in a high-field imaging experiment. J Magn Reson Imag 2000;12(1):46–67.

[10] Setsompop K, Wald LL, Alagappan V, Gagoski BA, Adalsteinsson E. Magnitude least squares optimization for parallel radio frequency excitation design demonstrated at 7 Tesla with eight channels. Magn Reson Med 2008;59 (4):908–15.

[11] Cloos MA, Boulant N, Luong M, Ferrand G, Giacomini E, Le Bihan D, et al. kT-points: short three-dimensional tailored RF pulses for flip-angle homogenization over an extended volume. Magn Reson Med 2012;67(1):72–80.

[12] Malik SJ, Keihaninejad S, Hammers A, Hajnal JV. Tailored excitation in 3D with spiral nonselective (SPINS) RF pulses. Magn Reson med 2012;67 (5):1303–15.

[13] Gras V, Vignaud A, Amadon A, Le Bihan D, Boulant N. Universal pulses: a new concept for calibration-free parallel transmission. Magn Reson Med 2017;77 (2):635–43.

[14] Orzada S, Maderwald S, Poser BA, Bitz AK, Quick HH, Ladd ME. RF excitation using time interleaved acquisition of modes (TIAMO) to address B1 inhomogeneity in high-field MRI. Magn Reson Med 2010;64 (2):327–33.

[15] Haines K, Smith NB, Webb AG. New high dielectric constant materials for tailoring the B1+ distribution at high magnetic fields. J Magn Reson 2010;203 (2):323–7.

[16] Lagendijk JJW, Raaymakers BW, van Vulpen M. , The magnetic resonance imaging-linac system. Sem Radiat Oncol 2014;24(3):207–9.

[17] Sahgal A, Tseng C-L, Teng F, Parmar HA, Balter JM, Cao Y. MR-guided radiation therapy: transformative technology and its role in the central nervous system. Neuro-oncology 2017;19(suppl2):ii16–29.

[18] Hajnal J, Decoene B, Lewis P, Baudouin C, Cowan F, Pennock J, et al. High signal regions in normal white matter shown by heavily T2-weighted CSF nulled IR sequences. J Comput Assis Tomogr 1992;16(4):506–13.

[19] Niyazi M, Brada M, Chalmers AJ, Combs SE, Erridge SC, Fiorentino A, et al. ESTRO-ACROP guideline -target delineation of glioblastomas'. Radiother Oncol 2016;118(1):35–42.

[20] Visser F, Zwanenburg JJM, Hoogduin JM, Luijten PR. High-resolution magnetization-prepared 3D-FLAIR imaging at 7.0 Tesla. Magn Reson Med 2010(1):194–202.

[21] Regnery S, Knowles BR, Paech D, Behl N, Meissner J-E, Windisch P, et al. High-resolution FLAIR MRI at 7 Tesla for treatment planning in glioblastoma patients. Radiother Oncol MRI at 7 2019:180–4.

[22] Zwanenburg JJM, Hendrikse J, Visser F, Takahara T, Luijten PR. Fluid attenuated inversion recovery (FLAIR) MRI at 7.0 Tesla: comparison with 1.5 and 3.0 Tesla. Euro Radiol 2010;4:915–22.

[23] Beqiri A, Hoogduin H, Sbrizzi A, Hajnal JV, Malik SJ. Whole-brain 3D FLAIR at 7T using direct signal control. Magn Reson Med.

[24] Kilsdonk ID, De Graaf WL, Soriano AL, Zwanenburg JJ, Visser F, Kuijer JPA, et al. Multicontrast mr imaging at 7T in multiple sclerosis: highest lesion detection in cortical gray matter with 3D-FLAIR. Am J Neuroradiol 2013;4:791–6.

[25] Conolly S, Nishimura D, Macovski A, Glover G. Variable-rate selective excitation. J Magn Reson 1988;78(3):440–58. 1969.

[26] Hennig J, Scheffler K. Hyperechoes. Magn Reson Med: Off J Int Soc Magn Reson Med 2001;46(1):6–12.

[27] Mugler JP, Bao S, Mulkern RV, Guttmann CRG, Robertson RL, Jolesz FA, Brookeman JR. Optimized single-slab three-dimensional spin-echo MR imaging of the brain. Radiology 2000;216(3):891–9.

[28] Demuth T, Berens ME. Molecular mechanisms of glioma cell migration and invasion. J Neuro-oncol 2004;70(2):217–28.

[29] Compter I, Peerlings J, Eekers DBP, Postma AA, Ivanov D, Wiggins CJ, et al. Technical feasibility of integrating 7T anatomical MRI in image-guided radiotherapy of glioblastoma: a preparatory study. Magn Reson Mater Phys Biol Med 2016;29(3):591–603.

[30] Peerlings J, Compter I, Janssen F, Wiggins CJ, Postma AA, Mottaghy FM, et al. Characterizing geometrical accuracy in clinically optimised 7T and 3T magnetic resonance images for high-precision radiation treatment of brain tumours. Phys Imag Radiat Oncol 2019;9:35–42.

[31] Dammann P, Kraff O, Wrede KH, Zkan N, Orzada S, Mueller OM, et al. Evaluation of hardware-related geometrical distortion in structural MRI at 7 Tesla for image-guided applications in neurosurgery. Acad Radiol 2011;18 (7):910–6.

[32] Eisenhauer EA, Therasse P, Bogaerts J, Schwartz LH, Sargent D, Ford R, et al. New response evaluation criteria in solid tumours: revised RECIST guideline (version 1.1). Euro J Cancer 2009;45(2):228–47.

[33] Sharpton SR, Oermann EK, Moore DT, Schreiber E, Hoffman R, Morris DE, et al. The volumetric response of brain metastases after stereotactic radiosurgery and its post-treatment implications. Neurosurgery 2013;74(1):9–16.

[34] Law M, Young RJ, Babb JS, Peccerelli N, Chheang S, Gruber ML, et al. Gliomas: predicting time to progression or survival with cerebral blood volume measurements at dynamic susceptibility-weighted contrast-enhanced perfusion mr imaging. Radiology 2008;247(2):490–8.

[35] Chenevert TL, Stegman LD, Taylor JMG, Robertson PL, Greenberg HS, Rehemtulla A, et al. Diffusion magnetic resonance imaging: an early

[36] Scott JN, Brasher PMA, Sevick RJ, Rewcastle NB, Forsyth PA. How often are nonenhancing supratentorial gliomas malignant? A population study. Neurology 2002;59(6):947–9.

[37] Wen PY, Macdonald DR, Reardon DA, Cloughesy TF, Sorensen AG, Galanis E, et al. Updated response assessment criteria for high-grade gliomas: response assessment in neuro-oncology working group. J Clin Oncol 2010;28 (11):1963–72.

[38] Ellingson BM, Malkin MG, Rand SD, Connelly JM, Quinsey C, LaViolette PS, et al. Validation of functional diffusion maps (fDMs) as a biomarker for human glioma cellularity. J Magn Reson Imag: Off J Int Soc Magn Reson Med 2010;31(3):538–48.

[39] Sugahara T, Korogi Y, Kochi M, Ikushima I, Shigematu Y, Hirai T, et al. Usefulness of diffusion-weighted MRI with echo-planar technique in the evaluation of cellularity in gliomas. J Magn Reson Imag: Off J Int Soc Magn Reson Med 1999;9(1):53–60.

[40] Kono K, Inoue Y, Nakayama K, Shakudo M, Morino M, Ohata K, et al. The role of diffusion-weighted imaging in patients with brain tumors. Am J Neuroradiol 2001;22(6):1081–8.

[41] Gupta RK, Cloughesy TF, Sinha U, Garakian J, Lazareff J, Rubino G, et al. Relationships between choline magnetic resonance spectroscopy, apparent diffusion coefficient and quantitative histopathology in human glioma. J Neuro-oncol 2000;50(3):215–26.

[42] Mills SJ, Soh C, Rose CJ, Cheung S, Zhao S, Parker GJM, et al. Candidate biomarkers of extravascular extracellular space: a direct comparison of apparent diffusion coefficient and dynamic contrast-enhanced MR imaging-derived measurement of the volume of the extravascular extracellular space in glioblastoma multiforme. Am J Neuroradiol 2010;31(3):549–53.

[43] Moffat BA, Chenevert TL, Lawrence TS, Meyer CR, Johnson TD, Dong Q, et al. Functional diffusion map: a noninvasive MRI biomarker for early stratification of clinical brain tumor response. Proc Natl Acad Sci 2005;102(15):5524–9.

[44] Graaf D, Robin A. In Vivo NMR Spectroscopy: Principles and Techniques. Wiley; 2019.

[45] Gurney PT, Hargreaves BA, Nishimura DG. Design and analysis of a practical 3D cones trajectory. Magn Reson Med: Off J Int Soc Magn Reson Med 2006;55 (3):575–82.

[46] Qian Y, Boada FE. Acquisition-weighted stack of spirals for fast high-resolution three-dimensional ultra-short echo time MR imaging. Magn Reson Med 2008;60(1):135–45.

[47] Qian Y, Stenger VA, Boada FE. Parallel imaging with 3D TPI trajectory: SNR and acceleration benefits. Magn Reson Imag 2009;27(5):656–63.

[48] Nagel AM, Laun FB, Weber MA, Matthies C, Semmler W, Schad LR. Sodium MRI using a density-adapted 3D radial acquisition technique. Magn Reson Med 2009;62(6):1565–73.

[49] Riemer F, Solanky BS, Stehning C, Clemence M, Wheeler-Kingshott CAM, Golay X. Sodium (23Na) ultra-short echo time imaging in the human brain using a 3D-cones trajectory. Magn Reson Mater Phys Biol Med 2014;1:35–46.

[50] Robison RK, Anderson AG, Pipe JG. Three-dimensional ultrashort echo-time imaging using a FLORET trajectory. Magn Reson Med 2017(3):1038–49.

[51] Murphy E, Eisner DA. Regulation of intracellular and mitochondrial sodium in health and disease. Circul Res 2009;104(3):292–303.

[52] Thulborn KR, Davis D, Adams H, Gindin T, Zhou J. Quantitative tissue sodium concentration mapping of the growth of focal cerebral tumors with sodium magnetic resonance imaging. Magn Reson Med: Off J Int Soc Magn Reson Med 1999;41(2):351–9.

[53] Ouwerkerk R, Bleich KB, Gillen JS, Pomper MG, Bottomley PA. Tissue sodium concentration in human brain tumors as measured with 23Na MR imaging. Radiology 2003;227(2):529–37.

[54] Bartha R, Megyesi JF, Watling CJ. Low-grade glioma: correlation of short echo time 1H-MR spectroscopy with 23Na MR imaging. Am J Neuroradiol 2008;29 (3):464–70.

[55] Neto LPN, Madelin G, Sood TP, Wu C-C, Kondziolka D, Placantonakis D, et al. Quantitative sodium imaging and gliomas: a feasibility study. Neuroradiology 2018:1–8.

[56] Reshkin SJ, Bellizzi A, Caldeira S, Albarani V, Malanchi I, Poignee M, et al. Na$^+$/H$^+$ exchanger-dependent intracellular alkalinization is an early event in malignant transformation and plays an essential role in the development of subsequent transformation-associated phenotypes. FASEB J: Off Publ Feder Am Soc Exp Biol 2000;14:2185–97.

[57] Thulborn KR, Lu A, Atkinson IC, Damen F, Villano JL. Quantitative sodium MR imaging and sodium bioscales for the management of brain tumors. Neuroimag Clin 2009;19(4):615–24.

[58] Kline RP, Wu EX, Petrylak DP, Szabolcs M, Alderson PO, Weisfeldt ML, et al. Rapid in vivo monitoring of chemotherapeutic response using weighted sodium magnetic resonance imaging. Clin Cancer Res 2000;6(6):2146–56.

[59] Sharma R, Kline RP, Wu EX, Katz JK. Rapid in vivo taxotere quantitative chemosensitivity response by 4.23 Tesla sodium MRI and histo-immunostaining features in n-methyl-n-nitrosourea induced breast tumors in rats. Cancer Cell Int 2005;5(1):26.

[60] Thulborn KR, Lu A, Atkinson IC, Pauliah M, Beal K, Chan TA, et al. Residual tumor volume, cell volume fraction, and tumor cell kill during fractionated chemoradiation therapy of human glioblastoma using quantitative sodium mr imaging. Clin Cancer Res 2019;25(4):1226–32.

[61] Regnery S, Paech D, Schlemmer H-P, Ladd ME, Nagel AM, Rieken S, et al. 23Na MRI at 7 Tesla for early response assessment in patients with glioblastoma

and skull base meningioma. In: Europenne C, editor. Proceedings 26. Annual meeting international society for magnetic resonance in medicine, vol. 26. Paris, France; 2018. p. 4865. <http://archive.ismrm.org/2018/4865.html>.

[62] Warburg OH. Ueber den stoffwechsel der tumoren. J Springer; 1926.

[63] Miles KA, Williams RE. Warburg revisited: imaging tumour blood flow and metabolism. Cancer Imag 2008;8(1):81–6.

[64] Rigo P, Paulus P, Kaschten BJ, Hustinx R, Bury T, Jerusalem G, et al. Oncological applications of positron emission tomography with fluorine-18 fluorodeoxyglucose. Euro J Nucl Med 1996;23(12):1641–74.

[65] Delbeke D. Oncological applications of fdg pet imaging: brain tumors, colorectal cancer lymphoma and melanoma. J Nucl Med 1999;40(4):591–603.

[66] Haberkorn U, Strauss LG, Dimitrakopoulou A, Engenhart R, Oberdorfer F, Ostertag H, et al. Pet studies of fluorodeoxyglucose metabolism in patients with recurrent colorectal tumors receiving radiotherapy. J Nucl Med 1991;32(8):1485–90.

[67] Wahl RL, Zasadny K, Helvie M, Hutchins GD, Weber B, Cody R. Metabolic monitoring of breast cancer chemohormonotherapy using positron emission tomography: initial evaluation. J Clin Oncol 1993;11(11):2101–11.

[68] Jansson T, Westlin JE, Ahlstrm H, Lilja A, Längstrm B, Bergh J. Positron emission tomography studies in patients with locally advanced and/or metastatic breast cancer: a method for early therapy evaluation? J Clin Oncol 1995;13(6):1470–7.

[69] L.G Strauss Fluorine-18 deoxyglucose and false-positive results: a major problem in the diagnostics of oncological patients 1996;(10):1409–5.

[70] Frackowiak R, Lenzi G-L, Jones T, Heather JD. Quantitative measurement of regional cerebral blood flow and oxygen metabolism in man using 15O and positron emission tomography: theory, procedure, and normal values. J Comput Assis Tomogr 1980;4(6):727–36.

[71] Mintun MA, Raichle ME, Martin WR, Herscovitch P. Brain oxygen utilization measured with O-15 radiotracers and positron emission tomography. J Nucl Med: Off Publ Nucl Med 1984;25(2):177–87.

[72] Rhodes CG, Wise RJS, Gibbs JM, Frackowiak RSJ, Hatazawa J, Palmer AJ, et al. In vivo disturbance of the oxidative metabolism of glucose in human cerebral gliomas. Ann Neurol: Off J Am Neurol Assoc Child Neurol Soc 1983;14(6):614–26.

[73] Ito M, Lammertsma AA, Wise RJS, Bernardi S, Frackowiak RSJ, Heather JD, et al. Measurement of regional cerebral blood flow and oxygen utilisation in patients with cerebral tumours using 15O and positron emission tomography: analytical techniques and preliminary results. Neuroradiology 1982;23(2):63–74.

[74] Mineura K, Yasuda T, Kowada M, Shishido F, Ogawa T, Uemura K. Positron emission tomographic evaluation of histological malignancy in gliomas using oxygen-15 and fluorine-18-fluorodeoxyglucose. Neurol Res 1986;8(3):164–8.

[75] Lammertsma AA, Wise RJS, Cox TCS, Thomas DGT, Jones T. Measurement of blood flow, oxygen utilisation, oxygen extraction ratio, and fractional blood volume in human brain tumours and surrounding oedematous tissue. Brit J Radiol 1985;58(692):725–34.

[76] Beaney RP, Brooks DJ, Leenders KL, Thomas DG, Jones T, Halnan KE. Blood flow and oxygen utilisation in the contralateral cerebral cortex of patients with untreated intracranial tumours as studied by positron emission tomography, with observations on the effect of decompressive surgery. J Neurol Neurosurg Psyc 1985;48(4):310–9.

[77] Tyler JL, Diksic M, Villemure JG, Evans AC, Meyer E, Yamamoto YL, et al. Metabolic and hemodynamic evaluation of gliomas using positron emission tomography. J Nucl Med 1987;28(7):1123–33.

[78] Alder F, Yu FC. On the spin and magnetic moment of O17. Phys Rev 1951;81(6):1067.

[79] Borowiak R, Groebner J, Haas M, Hennig J, Bock M. Direct cerebral and cardiac O-17-MRI at 3 Tesla: initial results at natural abundance. Magn Reson Mater Phys Biol Med 2014;27(1, SI):95–9.

[80] Hopkins AL, Barr RG. Oxygen-17 compounds as potential NMR T2 contrast agents: enrichment effects of H217O on protein solutions and living tissues. Magn Reson Med 1987;4(4):399–403.

[81] Arai T, Nakao S-I, Mori K, Ishimori K, Morishima I, Miyazawa T, et al. Cerebral oxygen utilization analyzed by the use of oxygen-17 and its nuclear magnetic resonance 1990;(1):153–8.

[82] Pekar J, Ligeti L, Ruttner Z, Lyon RC, Sinnwell TM, van Gerderen P, et al. In vivo measurement of cerebral oxygen consumption and blood flow using 17O magnetic resonance imaging. Magn Reson Med 1991;21(2):313–9.

[83] Fiat D, Dolinsek J, Hankiewicz J, Dujovny M, Ausman J. Determination of regional cerebral oxygen consumption in the human: 17O natural abundance cerebral magnetic resonance imaging and spectroscopy in a whole body system. Neurol Res 1993;15(4):237–48.

[84] Zhu XH, Zhang X, Zhang N, Zhang Y, Strupp J, Ugurbil K, et al. High-field 17O study of 3D CMRO2 imaging in human visual cortex. In: Proceedings 26. Annual meeting international society for magnetic resonance in medicine; 2006.

[85] Atkinson IC, Thulborn KR. Feasibility of mapping the tissue mass corrected bioscale of cerebral metabolic rate of oxygen consumption using 17-oxygen and 23-sodium MR imaging in a human brain at 9.4 T. Neuroimage 2010;51(2):723–33.

[86] Hoffmann SH, Radbruch A, Bock M, Semmler W, Nagel AM. Direct 17O MRI with partial volume correction: first experiences in a glioblastoma patient. Magn Reson Mater Phys Biol Med 2014;27(6):579–87.

[87] Hoffmann SH, Begovatz P, Nagel AM, Umathum R, Schommer K, Bachert P, et al. A measurement setup for direct (17)O MRI at 7 T. Magn Reson Med 2011;66(4):1109–15.

[88] Niesporek SC, Umathum R, Lommen JM, Behl NGR, Paech D, Bachert P, et al. Reproducibility of CMRO2 determination using dynamic O17. Magn Reson Med 2018;6:2923–34.

[89] Niesporek SC, Nagel AM, Umathum R, Behl NG, Ladd ME, Schlemmer H-P, et al. Metabolic rate of oxygen consumption in brain tumors: a pilot 17O-MRI study. In: Proceedings 26. Annual meeting international society for magnetic resonance in medicine, vol. 26, Paris, France; 2018. p. 0625. <http://archive.ismrm.org/2018/0625.html>.

[90] Song CW, Griffin R, Park HJ. Influence of tumor pH on therapeutic response. Springer; 2006. p. 21–42.

[91] Lu A, Atkinson IC, Zhou XJ, Thulborn KR. Pcr/atp ratio mapping of the human head by simultaneously imaging of multiple spectral peaks with interleaved excitations and flexible twisted projection imaging readout trajectories at 9.4 T. Magn Reson Med 2013;69(2):538–44.

[92] Steinseifer IK, Wijnen JP, Hamans BC, Heerschap A, Scheenen TWJ. Metabolic imaging of multiple x-nucleus resonances. Magn Reson Med 2013;70(1):169–75.

[93] Korzowski A, Bachert P. High-resolution 31P echo-planar spectroscopic imaging in vivo at 7T. Magn Reson Med.

[94] Qiao H, Zhang X, Zhu X-H, Du F, Chen W. In vivo 31P MRS of human brain at high/ultrahigh fields: a quantitative comparison of NMR detection sensitivity and spectral resolution between 4 T and 7 T. Magn Reson Imag 2006;24(10):1281–6.

[95] Kurhanewicz J, Thomas A, Jajodia P, Weiner MW, James TL, Vigneron DB, et al. 31P spectroscopy of the human prostate gland in vivo using a transrectal probe. Magn Reson Med 1991;22(2):404–13.

[96] R.A Komoroski, J.C. Holder, A.A Pappas, A.E. Finkbeiner. 31P NMR of phospholipid metabolites in prostate cancer and benign prostatic hyperplasia 2011;(4):911–3.

[97] Thomas MA, Narayan P, Kurhanewicz J, Jajodia P, James TL, Weiner MW. Detection of phosphorus metabolites in human prostates with a transrectal 31P NMR probe. J Magn Reson 1992;99(2):377–86.

[98] Narayan P, Jajodia P, Kurhanewicz J, Thomas A, MacDonald J, Hubesch B, et al. Characterization of prostate cancer, benign prostatic hyperplasia and normal prostates using transrectal 31phosphorus magnetic resonance spectroscopy: a preliminary report. J Urol 1991;146(1):66–74.

[99] Podo F. Tumour phospholipid metabolism, NMR in biomedicine: an international journal devoted to the development and application of magnetic resonance. In Vivo 1999;12(7):413–39.

[100] Klomp DWJ, Bitz AK, Heerschap A, Scheenen TWJ. Proton spectroscopic imaging of the human prostate at 7 T 2009;(5):495–501.

[101] Kobus T, Bitz AK, van Uden MJ, Lagemaat MW, Rothgang E, Orzada S, et al. In vivo 31P MR spectroscopic imaging of the human prostate at 7 T: safety and feasibility. Magn Reson Med 2012;68(6):1683–95.

[102] Luttje MP, Italiaander MGM, Arteaga De Castro CS, Van Der Kemp WJM, Luijten PR, Van Vulpen M, et al. 31P MR spectroscopic imaging combined with 1 H MR spectroscopic imaging in the human prostate using a double tuned endorectal coil at 7T 2014;(6):1516–21.

[103] Lagemaat MW, Vos EK, Maas MC, Bitz AK, Orzada S, van Uden MJ, et al. Phosphorus magnetic resonance spectroscopic imaging at 7 T in patients with prostate cancer. Investig Radiol 2014;49(5):363–72.

[104] Lagemaat MW, Maas MC, Vos EK, Bitz AK, Orzada S, Weiland E, et al. 31P MR spectroscopic imaging of the human prostate at 7 T: T1 relaxation times, nuclear overhauser effect, and spectral characterization. Magn Reson Med 2015;73(3):909–20.

[105] Avison MJ, Rothman DL, Nadel E, Shulman RG. Detection of human muscle glycogen by natural abundance 13C NMR. Proc Natl Acad Sci 1988;85(5):1634–6.

[106] Rothman DL, De Feyter HM, de Graaf RA, Mason GF, Behar KL. 13C MRS studies of neuroenergetics and neurotransmitter cycling in humans. NMR Biomed 2011;24(8):943–57.

[107] Terpstra M, Gruetter R, High WB, Mescher M, DelaBarre L, Merkle H, et al. Lactate turnover in rat glioma measured by in vivo nuclear magnetic resonance spectroscopy. Cancer Res 1998;58(22):5083–8.

[108] Wijnen JP, Van der Graaf M, Scheenen TWJ, Klomp DWJ, de Galan BE, Idema AJS, et al. In vivo 13C magnetic resonance spectroscopy of a human brain tumor after application of 13C-1-enriched glucose. Magn Reson Imag 2010;28(5):690–7.

[109] Ardenkjaer-Larsen JH, Fridlund B, Gram A, Hansson G, Hansson L, Lerche MH, et al. Increase in signal-to-noise ratio of> 10,000 times in liquid-state NMR. Proc Natl Acad Sci 2003;100(18):10158–63.

[110] Bowers CR, Weitekamp DP. Parahydrogen and synthesis allow dramatically enhanced nuclear alignment. J Am Chem Soc 1987;109(18):5541–2.

[111] Park JM, Recht LD, Josan S, Merchant M, Jang Y-F, et al. Metabolic response of glioma to dichloroacetate measured in vivo by hyperpolarized 13C magnetic resonance spectroscopic imaging. Neuro-oncology 2013;15(4):433–41.

[112] Nelson SJ, Kurhanewicz J, Vigneron DB, Larson PEZ, Harzstark AL, Ferrone M, et al. Metabolic imaging of patients with prostate cancer using hyperpolarized [1-13c]pyruvate. Sci Transl Med 2013;5(198):198ra108.

[113] Day SE, Kettunen MI, Gallagher FA, Hu D-E, Lerche M, Wolber J, et al. Detecting tumor response to treatment using hyperpolarized 13C magnetic resonance imaging and spectroscopy. Nat Med 2007;13:1382.

[114] Park JM, Spielman DM, Josan S, Jang T, Merchant M, Hurd RE, et al. Hyperpolarized 13C-lactate to 13C-bicarbonate ratio as a biomarker for monitoring the acute response of anti-vascular endothelial growth factor (anti-VEGF) treatment. NMR Biomed 2016;29(5):650–9.

[115] V.C. Sandulache, Y. Chen, J. Lee, A. Rubinstein, M.S. Ramirez, H.D. Skinner, C.M. Walker, M.D. Williams, R. Tailor, L.E. Court, J.A. Bankson, S.Y. Lai, Evaluation of hyperpolarized [1-13c]-pyruvate by magnetic resonance to detect ionizing radiation effects in real time (1) (2014) e87031.

[116] Schoenheimer R, Rittenberg D. Deuterium as an indicator in the study of intermediary metabolism. 1. J Biol Chem 1935;111:163–8.

[117] Lu M, Zhu X-H, Zhang Y, Mateescu G, Chen W. Quantitative assessment of brain glucose metabolic rates using in vivo deuterium magnetic resonance spectroscopy. J Cereb Blood Flow Metab 2017;37(11):3518–30.

[118] De Feyter HM, Behar KL, Corbin ZA, Fulbright RK, Brown PB, McIntyre S, et al. Deuterium metabolic imaging (DMI) for MRI-based 3D mapping of metabolism in vivo. Sci Adv 2018;4(8):eaat7314.

[119] Wu B, Warnock G, Zaiss M, Lin C, Chen M, Zhou Z, et al. An overview of CEST MRI for non-mr physicists. EJNMMI Phys 2016;3(1):19.

[120] Zhou J, Payen J-F, Wilson DA, Traystman RJ, Van Zijl PCM. Using the amide proton signals of intracellular proteins and peptides to detect pH effects in MRI. Nat Med 2003;9(8):1085.

[121] Jones CK, Huang A, Xu J, Edden RAE, Schär M, Hua J, et al. Nuclear overhauser enhancement (NOE) imaging in the human brain at 7T. NeuroImage 2013;77:114–24.

[122] Togao O, Yoshiura T, Keupp J, Hiwatashi A, Yamashita K, Kikuchi K, et al. Amide proton transfer imaging of adult diffuse gliomas: correlation with histopathological grades. Neuro-oncology 2013;16(3):441–8.

[123] Paech D, Burth S, Windschuh J, Meissner J-E, Zaiss M, Eidel O, et al. Nuclear overhauser enhancement imaging of glioblastoma at 7 Tesla: Region specific correlation with apparent diffusion coefficient and histology 2015;(3): e0121220.

[124] Zaiss M, Windschuh J, Paech D, Meissner J-E, Burth S, Schmitt B, et al. Relaxation-compensated CEST-MRI of the human brain at 7 T: unbiased insight into noe and amide signal changes in human glioblastoma. Neuroimage 2015;112:180–8.

[125] Togao O, Hiwatashi A, Yamashita K, Kikuchi K, Keupp J, Yoshimoto K, et al. Grading diffuse gliomas without intense contrast enhancement by amide proton transfer MR imaging: comparisons with diffusion-and perfusion-weighted imaging. Europ Radiol 2017;27(2):578–88.

[126] Heo H, Jones CK, Hua J, Yadav N, Agarwal S, Zhou J, et al. Whole-brain amide proton transfer (APT) and nuclear overhauser enhancement (NOE) imaging in glioma patients using low-power steady-state pulsed chemical exchange saturation transfer (CEST) imaging at 7T. J Magn Reson Imag 2016;44 (1):41–50.

[127] Paech D, Windschuh J, Oberhollenzer J, Dreher C, Sahm F, Meissner J-E, et al. Assessing the predictability of idh mutation and mgmt methylation status in glioma patients using relaxation-compensated multipool CEST MRI at 7.0 T. Neuro-oncology 2018;20(12):1661–71.

[128] Jiang S, Zou T, Eberhart CG, Villalobos MAV, Heo H, Zhang Y, et al. Predicting idh mutation status in grade ii gliomas using amide proton transfer-weighted (APTw) MRI. Magn Reson Med 2017;78(3):1100–9.

[129] Dula AN, Arlinghaus LR, Dortch RD, Dewey BE, Whisenant JG, Ayers GD, et al. Amide proton transfer imaging of the breast at 3 T: establishing reproducibility and possible feasibility assessing chemotherapy response. Magn Reson Med 2013;70(1):216–24.

[130] Zhou J, Tryggestad E, Wen Z, Lal B, Zhou T, Grossman R, et al. Differentiation between glioma and radiation necrosis using molecular magnetic resonance imaging of endogenous proteins and peptides. Nat Med 2011;17(1):130.

[131] Mehrabian H, Myrehaug S, Soliman H, Sahgal A, Stanisz GJ. Evaluation of glioblastoma response to therapy with chemical exchange saturation transfer. Int J Radiat Oncol Biol Phys 2018;101(3):713–23.

[132] Meissner J-E, Korzowski A, Regnery S, Goerke S, Breitling J, Floca RO, et al. Early response assessment of glioma patients to definitive chemoradiotherapy using chemical exchange saturation transfer imaging at 7 T. J Magn Reson Imag, in press.

[133] Regnery S, Adeberg S, Dreher C, Oberhollenzer J, Meissner J-E, Goerke S, et al. Chemical exchange saturation transfer MRI serves as predictor of early progression in glioblastoma patients. Oncotarget 2018;9(47):28772–83.

[134] Sagiyama K, Mashimo T, Togao O, Vemireddy V, Hatanpaa KJ, Maher EA, et al. In vivo chemical exchange saturation transfer imaging allows early detection of a therapeutic response in glioblastoma. Proc Natl Acad Sci 2014:201323855.

[135] Desmond KL, Mehrabian H, Chavez S, Sahgal A, Soliman H, Rola R, et al. Chemical exchange saturation transfer for predicting response to stereotactic radiosurgery in human brain metastasis. Magn Reson Med 2017;78 (3):1110–20.

[136] Paech D, Dreher C, Regnery S, Meissner J-E, Goerke S, Windschuh J, et al. Relaxation-compensated amide proton transfer (APT) MRI signal intensity is associated with survival and progression in high-grade glioma patients. Euro Radiol 2019:1–11.

[137] Chan KWY, McMahon MT, Kato Y, Liu G, Bulte JWM, Bhujwalla ZM, et al. Natural d-glucose as a biodegradable MRI contrast agent for detecting cancer. Magn Reson Med 2012;68(6):1764–73.

[138] Rivlin M, Horev J, Tsarfaty I, Navon G. Molecular imaging of tumors and metastases using chemical exchange saturation transfer (CEST) MRI. Sci Rep 2013;3:3045.

[139] Walker-Samuel S, Ramasawmy R, Torrealdea F, Rega M, Rajkumar V, Johnson SP, et al. In vivo imaging of glucose uptake and metabolism in tumors. Nat Med 2013;19:1067.

[140] Jin T, Mehrens H, Hendrich KS, Kim S-G. Mapping brain glucose uptake with chemical exchange-sensitive spin-lock magnetic resonance imaging. J Cereb Blood Flow Metabol 2014;34(8):1402–10.

[141] Schuenke P, Koehler C, Korzowski A, Windschuh J, Bachert P, Ladd ME, et al. Adiabatically prepared spin-lock approach for T1-based dynamic glucose enhanced MRI at ultrahigh fields. Magn Reson Med 2017;78(1):215–25.

[142] Paech D, Schuenke P, Koehler C, Windschuh J, Mundiyanapurath S, Bickelhaupt S, et al. T1-weighted dynamic glucose-enhanced MR imaging in the human brain. Radiology 2017;285(3):914–22.

[143] Schuenke P, Paech D, Koehler C, Windschuh J, Bachert P, Ladd ME, et al. Fast and quantitative T1-weighted dynamic glucose enhanced MRI. Sci Rep 2017;7:42093.

[144] Xu X, Yadav NN, Knutsson L, Hua J, Kalyani R, Hall E, et al. Dynamic glucose-enhanced (DGE) MRI: translation to human scanning and first results in glioma patients. Tomography 2015;1(2):105.

[145] Keall PJ, Mageras GS, Balter JM, Emery RS, Forster KM, Jiang SB, et al. The management of respiratory motion in radiation oncology report of aapm task group 76a). Med Phys 2006;33(10):3874–900.

[146] Timmerman R, McGarry R, Yiannoutsos C, Papiez L, Tudor K, DeLuca J, et al. Excessive toxicity when treating central tumors in a phase II study of stereotactic body radiation therapy for medically inoperable early-stage lung cancer. J Clin Oncol 2006;24(30):4833–9. Available from: arXiv: NIHMS150003.

[147] Chang DT, Swaminath A, Kozak M, Weintraub J, Koong AC, Kim J, et al. Stereotactic body radiotherapy for colorectal liver metastases: a pooled analysis. Cancer 2011;117(17):4060–9.

[148] Lax I, Blomgren H, Näslund I, Svanstrm R. Stereotactic radiotherapy of malignancies in the abdomen: methodological aspects. Acta Oncol 1994;33 (6):677–83.

[149] Shirato H, Shimizu S, Kunieda T, Kitamura K, Van Herk M, Kagei K, et al. Physical aspects of a real-time tumor-tracking system for gated radiotherapy. Int J Radiat Oncol Biol Phys 2000;48(4):1187–95.

[150] Bert C, Metheany KG, Doppke K, Chen GTY. A phantom evaluation of a stereo-vision surface imaging system for radiotherapy patient setup. Med Phys 2005;32(9):2753–62.

[151] Ramsey CR, Scaperoth D, Arwood D. Clinical experience with a commercial respiratory gating system. Int J Radiat Oncol Biol Phys 2000;48(3):164–5.

[152] Feng M, Balter JM, Normolle D, Adusumilli S, Cao Y, Chenevert TL, et al. Characterization of pancreatic tumor motion using cine MRI: surrogates for tumor position should be used with caution. Int J Radiat Oncol Biol Phys 2009;74(3):884–91.

[153] Park S, Farah R, Shea SM, Tryggestad E, Hales R, Lee J. Simultaneous tumor and surrogate motion tracking with dynamic MRI for radiation therapy planning. Phys Med Biol 2018;63(2):025015.

[154] Murphy MJ. Tracking moving organs in real time, vol. 14. Elsevier; 2004. pp. 91–100.

[155] Chen Q, Weinhous MS, Deibel FC, Ciezki JP, Macklis RM. Fluoroscopic study of tumor motion due to breathing: facilitating precise radiation therapy for lung cancer patients. Med Phys 2001;28(9):1850–6.

[156] Dempsey J, Benoit D, Fitzsimmons J, Haghighat A, Li J, Low D, et al. A device for realtime 3D image-guided imrt. Int J Rad Oncol Biol Phys 2005;63:S202.

[157] Mutic S, Dempsey JF. The viewray system: magnetic resonance-guided and controlled radiotherapy. Seminars Radiat Oncol 2014;24(3):196–9.

[158] Lagendijk J, Raaymakers B, van der Heide U, Overweg J, Brown K, Bakker C, et al. Mo-e-j-6b-03: in room magnetic resonance imaging guided radiotherapy (MRIgRT). Med Phys 2005;32(6Part14):2067.

[159] Raaymakers BW, Lagendijk JJW, Overweg J, Kok JGM, Raaijmakers AJE, Kerkhof EM, et al. Integrating a 1.5 T MRI scanner with a 6 MV accelerator: proof of concept. Phys Med Biol 2009;54(12):N229–37.

[160] Raaymakers BW, De Boer JCJ, Knox C, Crijns SPM, Smit K, Stam MK, et al. Integrated megavoltage portal imaging with a 1.5 T MRI linac 2011; (19): N207–N214.

[161] Fallone B, Carlone M, Murray B, Rathee S, Stanescu T, Steciw S, et al. Tu-c-m100f-01: development of a linac-MRI system for real-time ART. Med Phys 2007;34(6Part17):2547.

[162] Fallone BG. The rotating biplanar linac-magnetic resonance imaging system. Sem Radiat Oncol 2014;24(3):200–2.

[163] Keall PJ, Barton M, Crozier S. The australian magnetic resonance imaging-linac program. Sem Radiat Oncol 2014;24(3):203–6.

[164] Liney GP, Dong B, Begg J, Vial P, Zhang K, Lee F, et al. Technical note: experimental results from a prototype high-field inline MRI-linac 2016; (9): 5188–94.

[165] Mansfield P, Harvey PR, Stehling MK. Echo-volumar imaging. Magn Reson Mater Phys Biol Med 1994;2(3):291–4.

[166] Tisdall MD, Hess AT, Reuter M, Meintjes EM, Fischl B, van der Kouwe AJW. Volumetric navigators for prospective motion correction and selective reacquisition in neuroanatomical MRI. Magn Reson Med 2012;68(2):389–99.

[167] Poser BA, Koopmans PJ, Witzel T, Wald LL, Barth M. Three dimensional echo-planar imaging at 7 Tesla. Neuroimage 2010;51(1):261–6.

[168] Posse S, Ackley E, Mutihac R, Zhang T, Hummatov R, Akhtari M, et al. High-speed real-time resting-state fMRI using multi-slab echo-volumar imaging. Front Human Neurosci 2013;7:479.

[169] Feng L, Srichai MB, Lim RP, Harrison A, King W, Adluru G, et al. Highly accelerated real-time cardiac cine MRI using k-t SPARSE-SENSE. Magn Reson Med 2013;70(1):64–74.

[170] Razavi R, Hill DLG, Keevil SF, Miquel ME, Muthurangu V, Hegde S, et al. Cardiac catheterisation guided by MRI in children and adults with congenital heart disease. Lancet 2003;362(9399):1877–82.

[171] Boutin RD, Buonocore MH, Immerman I, Ashwell Z, Sonico GJ, Szabo RM, et al. Real-time magnetic resonance imaging (MRI) during active wrist motion–initial observations. PloS One 2013;8(12):e84004.

[172] Narayanan S, Nayak K, Lee S, Sethy A, Byrd D. An approach to real-time magnetic resonance imaging for speech production. J Acoust Soc Am 2004;115(4):1771–6.

[173] Scheffler K, Lehnhardt S. Principles and applications of balanced SSFP techniques. Euro Radiol 2003;13(11):2409–18.

[174] Plathow C, Ley S, Fink C, Puderbach M, Hosch W, Schmähl A, et al. Analysis of intrathoracic tumor mobility during whole breathing cycle by dynamic MRI. Int J Radiat Oncol Biol Phys 2004;59:952–9.

[175] Cervio LI, Du J, Jiang SB. MRI-guided tumor tracking in lung cancer radiotherapy. Phys Med Biol 2011;56:3773–85.

[176] Fischer-Valuck BW, Henke L, Green O, Kashani R, Acharya S, Bradley JD, et al. Two-and-a-half-year clinical experience with the world's first magnetic resonance image guided radiation therapy system. Adv Radiat Oncol 2017;2 (3):485–93.

[177] Bjerre T, Crijns S, Rosenschld PMA, Aznar M, Specht L, Larsen R, et al. Three-dimensional MRI-linac intra-fraction guidance using multiple orthogonal cine-MRI planes. Phys Med Biol 2013;58(14):4943–50.

[178] Seregni M, Paganelli C, Lee D, Greer PB, Baroni G, Keall PJ, et al. Motion prediction in MRI-guided radiotherapy based on interleaved orthogonal cine-MRI 61(2); 872–87.

[179] Kontaxis C, Bol GH, Stemkens B, Glitzner M, Prins FM, Kerkmeijer LG, Lagendijk JJ, Raaymakers BW. Towards fast online intrafraction replanning for free-breathing stereotactic body radiation therapy with the MR-linac. Phys Med Biol 2017;62(18):7233–48.

[180] Stam MK, Crijns SPM, Zonnenberg BA, Barendrecht MM, van Vulpen M, Lagendijk JJW, et al. Navigators for motion detection during real-time MRI-guided radiotherapy. Phys Med Biol 2012;57(21):6797–805.

[181] Crijns SPM, Raaymakers BW, Lagendijk JJW. Proof of concept of MRI-guided tracked radiation delivery: tracking one-dimensional motion. Phys Med Biol 2012;57(23):7863.

[182] Raaymakers BW, Jürgenliemk-Schulz IM, Bol GH, Glitzner M, Kotte ANTJ, van Asselen B, et al. First patients treated with a 1.5T MRI-linac: clinical proof of concept of a high-precision, high-field mri guided radiotherapy treatment. Phys Med Biol 2017;62(23):L41.

[183] Zhang S, Block KT, Frahm J. Magnetic resonance imaging in real time: advances using radial FLASH. J Magn Reson Imag 2010;31(1):101–9.

[184] Uecker M, Zhang S, Voit D, Karaus A, Merboldt K, Frahm J. Real-time MRI at a resolution of 20 ms. NMR Biomed 2010;23(8):986–94.

[185] Winkelmann S, Schaeffter T, Koehler T, Eggers H, Doessel O. An optimal radial profile order based on the golden ratio for time-resolved MRI. IEEE Trans Med Imag 2007;26(1):68–76.

[186] Voit D, Zhang S, Unterberg-Buchwald C, Sohns JM, Lotz J, Frahm J. Real-time cardiovascular magnetic resonance at 1.5 T using balanced SSFP and 40 ms resolution. J Cardiovasc Magn Reson 2013;15(1):1–8.

[187] Vaals V, Joop J, Brummer ME, Thomas Dixon W, Tuithof HH, Engels H, et al. 'Keyhole' method for accelerating imaging of contrast agent uptake. J Magn Reson Imag 1993;3(4):671–5.

[188] Lee D, Pollock S, Whelan B, Keall P, Kim T. Dynamic keyhole: a novel method to improve mr images in the presence of respiratory motion for real-time mri. Med Phys 2014;41(7):072304.

[189] Korosec FR, Frayne R, Grist TM, Mistretta CA. Time-resolved contrast-enhanced 3D MR angiography. Magn Reson Med 1996;36(3):345–51.

[190] Fink C, Puderbach M, Ley S, Zaporozhan J, Plathow C, Kauczor H-U. Time-resolved echo-shared parallel MRA of the lung: observer preference study of image quality in comparison with non-echo-shared sequences. Euro Radiol 2005;15(10):2070–4.

[191] Plathow C, Schoebinger M, Fink C, Hof H, Debus J, Meinzer H-P, et al. Quantification of lung tumor volume and rotation at 3D dynamic parallel MR imaging with view sharing: preliminary results. Radiology 2006;240(2):537–45.

[192] Dinkel J, Hintze C, Tetzlaff R, Huber PE, Herfarth K, Debus J, et al. 4D-MRI analysis of lung tumor motion in patients with hemidiaphragmatic paralysis. Radiother Oncol 2009;91(3):449–54.

[193] Friedrich F, Klüter S, Spindeldreier K, Mann P, Ladd ME, Bachert P, Knowles BR. Motion-adaptive temporal resolution for radial real-time imaging at a low field MR-linac. In: Europenne C, editor. Proceedings 27. Annual meeting international society for magnetic resonance in medicine, vol. 27. Montreal, Canada; 2019. p. 4865.

[194] Pruessmann KP, Weiger M, Scheidegger MB, Boesiger P. Sense: sensitivity encoding for fast MRI. Magn Reson Med 1999;42(5):952–62.

[195] Tsao J, Boesiger P, Pruessmann KP. k-t blast and k-t sense: dynamic mri with high frame rate exploiting spatiotemporal correlations. Magn Reson Med: Off J Int Soc Magn Reson Med 2003;50(5):1031–42.

[196] Kellman P, Epstein FH, McVeigh ER. Adaptive sensitivity encoding incorporating temporal filtering (TSENSEe). Magn Reson Med: Off J Int Soc Magn Reson Med 2001;45(5):846–52.

[197] Hansen MS, Atkinson D, Sorensen TS. Cartesian sense and k-t sense reconstruction using commodity graphics hardware. Magn Reson Med: Off J Int Soc Magn Reson Med 2008;59(3):463–8.

[198] Roujol S, de Senneville BD, Vahala E, Sürensen TS, Moonen C, Ries M. Online real-time reconstruction of adaptive tsense with commodity cpu/gpu hardware. Magn Reson Med: Off J Int Soc Magn Reson Med 2009;62 (6):1658–64.

[199] Sørensen TS, Atkinson D, Schaeffter T, Hansen MS. Real-time reconstruction of sensitivity encoded radial magnetic resonance imaging using a graphics processing unit. IEEE Trans Med Imag 2009;28(12):1974–85.

[200] Saybasili H, Herzka DA, Seiberlich N, Griswold MA. Real-time imaging with radial grappa: Implementation on a heterogeneous architecture for low-latency reconstructions. Magn Reson Imag 2014;32(6):747–58.

[201] Uecker M, Zhang S, Frahm J. Nonlinear inverse reconstruction for real-time MRI of the human heart using undersampled radial flash. Magn Reson Med 2010;63(6):1456–62.

[202] Yun J, Yip E, Wachowicz K, Rathee S, Mackenzie M, Robinson D, et al. Evaluation of a lung tumor autocontouring algorithm for intrafractional tumor tracking using low-field MRI: a phantom study. Med Phys 2012;39 (3):1481–94.

[203] Yun J, Wachowicz K, Mackenzie M, Rathee S, Robinson D, Fallone BG. First demonstration of intrafractional tumor-tracked irradiation using 2D phantom mr images on a prototype linac-MR. Med Phys 2013;40 (5):051718.

[204] Yun J, Yip E, Gabos Z, Wachowicz K, Rathee S, Fallone BG. Neural-network based autocontouring algorithm for intrafractional lung-tumor tracking using Linac-MR. Med Phys 2015;42(5):2296–310.

[205] Feng Y, Kawrakow I, Olsen J, Parikh PJ, Noel C, Wooten O, et al. A comparative study of automatic image segmentation algorithms for target tracking in MR-IGRT. J Appl Clin Med Phys 2016;17(2):441–60.

[206] Gou S, Lee P, Hu P, Rwigema J-C, Sheng K. Feasibility of automated 3-dimensional magnetic resonance imaging pancreas segmentation. Adv Radiat Oncol 2016;1(3):182–93.

[207] Bourque AE, Bedwani S, Filion, Carrier J. A particle filter based autocontouring algorithm for lung tumor tracking using dynamic magnetic resonance imaging. Med Phys 2016;43(9):5161–9.

[208] Bourque AE, Carrier J-F, Filion d, Bedwani S. A particle filter motion prediction algorithm based on an autoregressive model for real-time MRI-guided radiotherapy of lung cancer. Biomed Phys Eng Exp 2017;3 (3):035001.

[209] Fast MF, Eiben B, Menten MJ, Wetscherek A, Hawkes DJ, McClelland JR, et al. Tumour auto-contouring on 2D cine MRI for locally advanced lung cancer: a comparative study. Radiother Oncol: J Euro Soc Therapeut Radiol Oncol 2017;125(3):485–91.

[210] Fu Y, Mazur TR, Wu X, Liu S, Chang X, Lu Y, et al. A novel segmentation method using CNN-based correction network for MRI-guided adaptive radiotherapy 45(11); 5129–5137.

[211] Tryggestad E, Flammang A, Hales R, Herman J, Lee J, McNutt T, et al. 4D tumor centroid tracking using orthogonal 2D dynamic MRI: implications for radiotherapy planning. Med Phys 40(9).

[212] Shi X, Diwanji T, Mooney KE, Lin J, Feigenberg S, D'souza WD, et al. Evaluation of template matching for tumor motion management with cine-MR images in lung cancer patients. Med Phys 2014;41(5):052304.

[213] Menten MJ, Fast MF, Wetscherek A, Rank CM, Kachelrie M, Collins DJ, et al. The impact of 2D cine MR imaging parameters on automated tumor and organ localization for mr-guided real-time adaptive radiotherapy. Phys Med Biol 2018;63(23):235005.

[214] Brix L, Ringgaard S, Sørensen TS, Poulsen PR. Three-dimensional liver motion tracking using real-time two-dimensional MRI. Med Phys 41(4).

[215] A. Silvia, I. Francesca,. Global respiratory motion model based on 4D CT and 2D cine-MRI.

[216] Yuan A, Wei J, Gaebler CP, Huang H, Olek D, Li G. A novel respiratory motion perturbation model adaptable to patient breathing irregularities. Int J Radiat Oncol Biol Phys 2016;96(5):1087–96.

[217] Wilms M, Ha IY, Handels H, Heinrich MP. Model-based regularisation for respiratory motion estimation with sparse features in image-guided interventions. Springer; 2016. p. 89–97.

[218] Harris W, Yin F-F, Wang C, Zhang Y, Cai J, Ren L. Accelerating volumetric cine MRI (VC-MRI) using undersampling for real-time 3D target localization/tracking in radiation therapy: a feasibility study. Phys Med Biol 2017;63(1):01NT01.

[219] Ha IY, Wilms M, Handels H, Heinrich MP. Model-based sparse-to-dense image registration for realtime respiratory motion estimation in image-guided interventions. IEEE Trans Biomed Eng 2019;66(2):302–10.

[220] Ginn JS, O'Connell D, Thomas DH, Low DA, Lamb JM. Model-interpolated gating for magnetic resonance image-guided radiation therapy. Int J Radiat Oncol Biol Phys 2018;102(4):885–94.

[221] Cejnek M, Bukovsky I, Homma N, Liska O. Adaptive polynomial filters with individual learning rates for computationally efficient lung tumor motion prediction. IEEE; 2015. p. 1–5.

[222] Bukhari W, Hong SM. Real-time prediction and gating of respiratory motion in 3D space using extended Kalman filters and gaussian process regression network. Phys Med Biol 2016;61(5):1947.

[223] Yun J, Mackenzie M, Rathee S, Robinson D, Fallone BG, An artificial neural network (ANN)-based lung-tumor motion predictor for intrafractional MR tumor tracking 2012;(7):4423.

[224] Lee SJ, Motai Y, Weiss E, Sun SS. Customized prediction of respiratory motion with clustering from multiple patient interaction. ACM Trans Intell Syst Technol (TIST) 2013;4(4):69.

[225] Thwaites DI, Tuohy JB. Back to the future: the history and development of the clinical linear accelerator. Phys Med Biol 2006;51(13):R343–62.